PHYSICAL REVIEW E **107**, 055208 (2023)

Ring structural transitions in strongly coupled dusty plasmas

Vikram Dharodi [*] and Evdokiya Kostadinova [†]
Department of Physics, Auburn University, Auburn, Alabama 32849, USA

(Received 24 February 2023; accepted 21 March 2023; published 16 May 2023)

This paper presents a numerical study of ring structural transitions in strongly coupled dusty plasma confined in a ring-shaped (quartic) potential well with a central barrier, whose axis of symmetry is parallel to the gravitational attraction. It is observed that increasing the amplitude of the potential leads to a transition from a ring monolayer structure (rings of different diameters nested within the same plane) to a cylindrical shell structure (rings of similar diameter aligned in parallel planes). In the cylindrical shell state, the ring's alignment in the vertical plane exhibits hexagonal symmetry. The ring transition is reversible, but exhibits hysteresis in the initial and final particle positions. As the critical conditions for the transitions are approached, the transitional structure states exhibit zigzag instabilities or asymmetries on the ring alignment. Furthermore, for a fixed amplitude of the quartic potential that results in a cylinder-shaped shell structure, we show that additional rings in the cylindrical shell structure can be formed by decreasing the curvature of the parabolic potential well, whose axis of symmetry is perpendicular to the gravitational force, increasing the number density, and lowering the screening parameter. Finally, we discuss the application of these findings to dusty plasma experiments with ring electrodes and weak magnetic fields.

DOI: 10.1103/PhysRevE.107.055208

I. INTRODUCTION

Complex (or dusty) plasmas are collections of nano-sized or micron-sized solid particles suspended in a plasma environment. Typically, the dust grains acquire negative charge and interact via the Yukawa (shielded Coulomb) potential. Depending on the coupling strength [1], the dusty plasma structure can be treated as a fluid [2,3], a visco-elastic fluid [4–7], or a crystal [8–11]. Variations of the coupling strength lead to phase or structure transitions [12–14] and control over the growth of instabilities (gravity driven [15,16] and shear driven [17–19]), turbulence [20–23], and wave propagation [24–26]), etc. In Earth-based experiments, due to the macroscopic size, the dust particles normally levitate close to the lower electrode, in the plasma sheath, where the gravitational force is balanced by the sheath electric force. In addition, the repulsive Yukawa interaction (the expansion) is commonly balanced by applying an external magnetic field [27–31] or by externally applied radial confinement potential [32], for example, due to a disk cutout or a ring placed on the lower electrode of a capacitively-coupled RF reference cell. Thus, the engineering of the vacuum chamber electrodes can be used to shape the confinement potentials in the plasma, which allows for the exploration of a wide range of structural and dynamical phenomena. For example, one-dimensional transverse optical modes have been investigated experimentally using horizontally aligned (perpendicular to gravity) dust chains confined in a harmonic potential created by a linear groove in the lower electrode [33]. The two-dimensional zigzag transitions have been studied in dusty plasmas confined by a biharmonic potential well created by a rectangular depression between four conducting bars placed on the RF powered electrode [34]. It has been shown that the properties of dust cluster rotation in a nonmagnetized dusty plasma is highly dependent on the characteristics of the parabolic radial confinement potential [35,36]. Numerical simulations of dusty plasma crystals confined in this type of potential have shown a transition from fully hexagonal structure to a structure with hexagonal lattice interior surrounded by concentric rings [37]. The formation of ring structure in dusty plasmas is of particular interest to the present study. A ring-shaped quadratic potential well has been used to numerically demonstrate the formation of complete and incomplete dust rings in the horizontal (perpendicular to gravity) plane [38,39]. Moreover, longitudinal and transverse dispersion relationships have been experimentally observed for this potential type [40]. A ring-shaped potential was formed using a circular grooved electrode with a center post and used to study a rotating ring of dust particles in a nonmagnetized plasma [41]. A rotating dust ring has also been observed within the ring-shaped asymmetric potential well created by asymmetric sawteeth of gears on the lower electrode [42]. Finally, it has been shown that in the presence of a weak magnetic field (about 150 G), the confinement potential of a ring placed on the lower electrode is modified, leading to the formation of a rotating ring dust structure [30].

Motivated by these experimental observations, here we use molecular dynamics (MD) simulations to explore ring

---

[*] vsd0005@auburn.edu
[†] egk003@auburn.edu

structural transitions for dust particles confined by a ring-shaped (quartic) potential well with a central barrier. Specifically, we investigate the critical conditions leading to a transition from a ring monolayer structure (rings of different diameters nested within the same plane) to a cylindrical shell structure (rings of similar diameter aligned in parallel planes). It is observed that the structural transition is governed by a competition between the strength of the Yukawa interaction potential and the properties of the external confinement potential. Thus, we conjecture that these ring transitions can be used to investigate dust particle charge in experiments where the shape of the double-well potential can be varied (for example, through changing the power on a ring electrode and the strength of an external magnetic field). In the present simulation, two types of external potentials have been employed: a ring-shaped quartic potential well providing the horizontal confinement and a parabolic potential well providing the vertical confinement. The axis of symmetry of the quartic potential is parallel to the gravitational force, whereas the parabolic potential is perpendicular to it. Before proceeding, here, it is also important to keep in mind that if the confinement/direction/plane is horizontal, it is perpendicular to gravity; if it is vertical, it is parallel to gravity.

For a fixed number of dust particles, the transition from a circular monolayer to a cylindrical shell structure is observed as the amplitude of the quartic potential is gradually increased. The transition is reversible and occurs through several intermediate transitional states. In these intermediate states, since the number of dust particles is either slightly higher or slightly lower than the requirement of ring formation number, these transition states exhibit a zigzag instability [43] or formation of uneven rings in both the horizontal and vertical directions. We observe that for an appropriate number of particles in the cylindrical shell phase (the number needed to form perfect rings for a given width of the annular potential well), the ring alignment in the vertical plane exhibits a hexagonal symmetry. For a fixed number of particles and a fixed amplitude of the quartic potential that supports a cylinder-shaped shell structure, decreasing the curvature of the parabolic potential (causes for the vertical confinement) results in the formation of additional rings in the cylindrical shell structure. This process occurs via several intermediary transition structures that exhibit irregularities only in the vertical direction. Similar observations have been made for simulations where the screening parameter is decreased and/or the dust number density is increased.

This paper is organized as follows. Section II presents the numerical scheme with a brief description of the external forces and potentials involved in our study. Section III is devoted to the numerical investigation of the structural transition phenomena followed by a detailed discussion of the obtained results. Finally, in Sec. IV, we provide a summary of our results and discuss applications of these findings. The CGS system of units is used in everything that follows.

II. MODEL AND METHODOLOGY

We consider a dusty plasma that includes N dust particles which interact through a Yukawa potential energy $\mathcal{U}^{ykw}$. Each particle has the same negative charge Q (in special circumstances like secondary electron emission [44] or nonneutral ion conditions, dust particles become positively charged [45,46]) and the same mass m_d. These particles are confined vertically with a parabolic potential energy $\mathcal{U}_z^{\text{ext}}$ as well as horizontally with a ring-shaped potential energy $\mathcal{U}_r^{\text{ext}}$. Therefore, the Hamiltonian $\mathcal{H}$ of the system can be expressed as

$$\mathcal{H} = \mathcal{K}_d + \mathcal{U}^{ykw} + \mathcal{U}_z^{\text{ext}} + \mathcal{U}_r^{\text{ext}}. \tag{1}$$

The Hamiltonian $\mathcal{H}$ is the sum of the kinetic energy $\mathcal{K}_d$, the interparticle interaction potential energy $\mathcal{U}^{ykw}$, and external potential energies $\mathcal{U}^{\text{ext}}$.

A. Yukawa interparticle interaction potential

The dust interparticle interaction is governed by a Yukawa potential of the form

$$U_{ij}^{ykw} = \frac{Q}{r_{ij}} exp(-r_{ij}/\lambda_D). \tag{2}$$

Here, r_{ij} is the radial distance between two particles and λ_D is the Debye length due to the background plasma [47]. Such a Yukawa system can be thermodynamically described by two dimensionless parameters: the screening parameter $\kappa = a/\lambda_D$ (i.e., the ratio of the inter-particle distance over the Debye length) and the unscreened Coulomb coupling parameter $\Gamma = Q^2/ak_BT_d$ (the ratio of interparticle Coulomb energy to the thermal kinetic energy); Here, the interparticle distance is given by $a = (3/4\pi n_d)^{1/3}$, n_d is the dust density, T_d is the dust temperature, and k_B is the Boltzmann constant.

B. Vertical confinement from a parabolic potential well

The simulation extends from 0 to lz along the vertical $\hat{z}$ direction. The external force due to gravity acts vertically downward

$$\mathbf{F}_z^g = m_d g(-\hat{z})$$

while the vertical upward electric force F_z^{ext} is given by

$$F_z^{\text{ext}} = QE_z^{\text{ext}}(\hat{z}).$$

Here we consider an electric field of the form

$$E_z^{\text{ext}} = E_{z0}(z - lz + c), \tag{3}$$

where $c < lz/2$ is a parameter that controls the curvature ("sharpness" and "depth") of the potential energy well. The larger the value of c, the sharper and deeper the curved potential well [see Fig. 1(a)]. In order to levitate the dust particles at an equilibrium vertical position $z = h$, the above two external forces should balance each other [48] at $z = h$, i.e.,

$$F_z^g = F_z^{\text{ext}} \text{ at } z = h.$$

Thus, the magnitude of the electric field at $z = h$ is given by

$$E_{z0} = \frac{m_d g}{Q} \frac{1}{(h - lz + c)}. \tag{4}$$

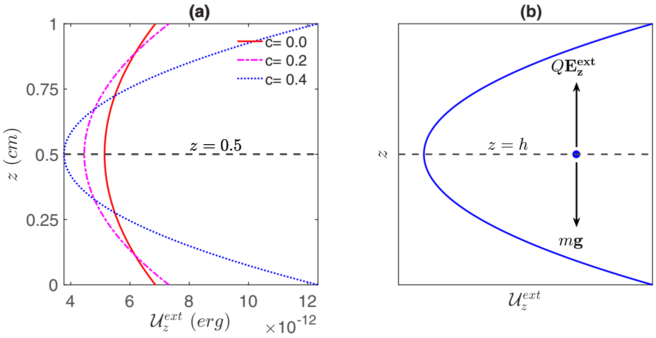

FIG. 1. The net parabolic potential energy diagram. Subplot (a) shows the potential energy $\mathcal{U}_z^{\text{ext}}$ as a function of z for several typical values of c and an equilibrium position $h = 0.5$ cm. Subplot (b) shows a schematic diagram for an equilibrium position $z = h$ (horizontal dotted line) for a particle (blue dot) where the gravitational force is balanced by the force due to the parabolic potential energy (blue solid curve).

The total potential energy associated with each particle at any vertical position z is

$$\mathcal{U}_z^{\text{ext}} = m_d g z + Q U_z^{\text{ext}} \tag{5}$$

and has contributions from the gravitational potential energy $m_d g z$ and the electrostatic energy QU_z^{ext} associated with the externally applied electric field E_z^{ext}. Here, $U_z^{\text{ext}} = -\int E_z^{\text{ext}} dz$. Therefore, the total potential energy becomes

$$\mathcal{U}_z^{\text{ext}} = m_d g z - E_{z0}\frac{(z - lz + c)^2}{2}. \tag{6}$$

This total potential energy has a parabolic shape with a symmetry axis perpendicular to gravity and centered on the equilibrium vertical position $z = h$. This parabolic potential is appropriate for modeling dust particles levitated near the plasma sheath in laboratory experiments [43,49,50]. The form of the potential selected here has been used to determine analytically the dust particle charge [51] and to simulate numerically structural transitions [14,52,53]. The potential energy diagram (z vs $\mathcal{U}_z^{\text{ext}}$) for several values of c is shown in Fig. 1(a), where $h = 0.5$ while the other parameters are fixed. This shows that as c increases, the walls of the potential well become steeper and the well becomes deeper without changing the vertical location of the minima $h = 0.5$. Thus, it is expected that a larger value of c will result in a decreased volume of vertical space available to levitate the dust particles. Later in the paper, we show how a decrease in the c value can be used to simulate the formation of additional rings in the cylindrical ring structure. A schematic diagram in Fig. 1(b) shows the equilibrium position for a particle (blue dot) along the horizontal dotted line at $z = h$ where the gravitational force is balanced by the confinement force due to the parabolic potential energy (blue solid curve).

C. Horizontal confinement from a ring-shaped potential well

In this work, we are interested in modeling experiments where a radial confinement potential traps the dust particle in a circular groove. For this we chose the following electric field profile

$$\mathbf{E}_r^{\text{ext}} = E_{r0}(x\hat{x} + y\hat{y})(r - d)(r + d), \tag{7}$$

where the horizontal plane is defined by the x axis and the y axis. Here, E_{r0} is the constant value of the radial electric field. The corresponding potential is

$$U_r^{\text{ext}} = -\frac{E_{r0}}{4}(r - d)^2(r + d)^2.$$

Therefore, the total radial potential energy associated with each negatively charged dust particle is

$$\mathcal{U}_r^{\text{ext}} = QU_r^{\text{ext}} = E_{r0}\frac{Q}{4}(r - d)^2(r + d)^2. \tag{8}$$

This quartic potential energy well is characterized by a ring of minimum energy at a radial distance $r = d$, a barrier centered at $r = 0$, and an axis of symmetry parallel to the gravitational attraction. Figure 2(a) shows a three dimensional (3D) view of this potential, while Fig. 2(c) shows a one dimensional (1D) projection. The corresponding force on a negatively charged dust particle is given by $\mathbf{F}_r^{\text{ext}} = Q\mathbf{E}_r^{\text{ext}}$:

$$\mathbf{F}_r^{\text{ext}} = QE_{r0}(x\hat{x} + y\hat{y})(r - d)(r + d). \tag{9}$$

$\mathbf{F}_r^{\text{ext}}$ is a radial vector force and has no tendency to swirl ($\nabla\times\mathbf{F}_r^{\text{ext}} = 0$). A schematic quiver plot of this radial force [Fig. 2(b)] shows that the force (as arrows) is pointing in the direction of minimum radial potential energy, i.e., $r = d$ (the blue solid circle). The arrowheads pointing outward (inside the circle) from the center represent the radially outward push on particles due to the central barrier, while the arrowheads pointing inward (outside the circle) represent the inward push due to the periphery of the potential. Thus, it is expected that, in this potential, the particles get trapped in a circular groove centered at radius $r = d$.

To illustrate how an increase in the quartic potential amplitude results in a ring structural transition, we have sketched the 1D profile (along x, at $y = 0$) of this potential in Fig. 2(c) for three different values of E_{r0}. It is evident that an increase in E_{r0} leads to steeper sides of the the well and a decreased radial space where the particles can levitate at a particular height $z = h$. Furthermore, Eq. (9) shows that higher E_{r0} results in greater radial force, which tends to squeeze the particles closer to the minima of the well. Starting with a small amplitude, $E_{r0} = low$, and fixed parameters for the vertical potential, we can introduce a sufficient number of dust particles to fill up the potential well and form a ring-shaped monolayer (coplanar nested rings of decreasing radius), radially centered around $r = d$ and vertically located at some $z = h$. The dust particles remain in-plane on the condition that, for the equilibrium interparticle spacing within the monolayer, the dust-dust interaction forces are balanced by the radial potential force and the gravitational force is balanced by the vertical parabolic potential force. As the amplitude of the radial confinement is increased to some intermediate value $E_{r0} = mid$, the dominance of the radial potential force over the dust-dust interactions will result in a structural state where these coplanner rings will show irregularities in the horizontal and vertical directions (i.e.,

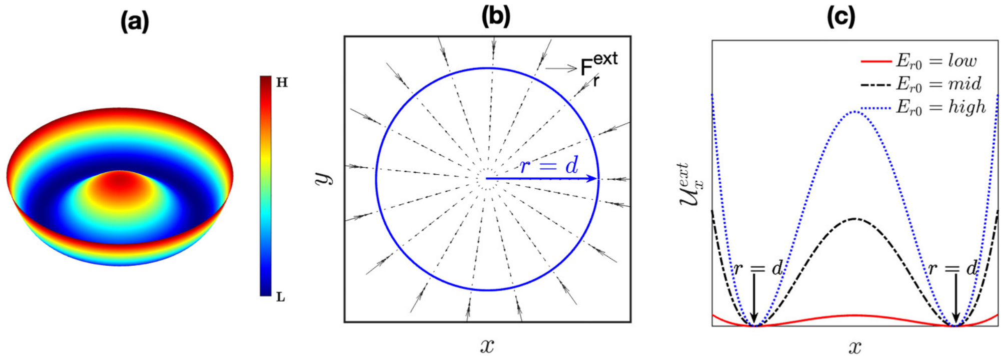

FIG. 2. Radial force and potential diagrams (not to scale). (a) A 3d schematic surface diagram of the quartic ring-shaped potential energy discussed in Eq. (8). The letter H that appears in the color bar is the acronym for the high-potential value region, while L stands for the low-potential region. (b) A schematic quiver plot of the radial force vector from Eq. (9). (c) A 1D projection of the 3D potential shown in (a) for three different values of E_{r0}.

transitional state). Finally, beyond a critical value of the amplitude, $E_{r0} = high$, new rings with the same diameter will form and align one above the other within a cylindrical surface with radius d (i.e., a cylindrical shell structure). The new force balance will result in a new interparticle separation within the cylindrical shell.

D. Governing equation

Including the interaction and confinement forces discussed above, the equation of motion of the ith dust particle for the Hamiltonian Eq. (1) can be written as

$$m_d\ddot{\mathbf{r}}_i = \mathbf{F}_{ij}^{ykw} + \mathbf{F}_r^{\text{ext}} + \mathbf{F}_z^{g} + \mathbf{F}_z^{\text{ext}}. \tag{10}$$

The right-hand side (RHS) of Eq. (10) is the sum of all the forces acting on the ith dust particle, which are given by

$$\begin{aligned}\mathbf{F}_{ij}^{ykw} &= -\nabla\sum_{i<j} U_{ij}^{ykw},\\ \mathbf{F}_r^{\text{ext}} &= +QE_r^{\text{ext}}\hat{r},\\ \mathbf{F}_z^{g} &= -m_d g\hat{z},\\ \mathbf{F}_z^{\text{ext}} &= +QE_z^{\text{ext}}\hat{z}.\end{aligned}$$

$\mathbf{F}_{ij}^{ykw}$ is the dust-dust interaction force, which is assumed to be a Yukawa (screened Coulomb). The following three force terms account for radial confinement, gravity, and vertical confinement. In each simulation case presented here, we first disperse N identical dust particles randomly in a 3D simulation box. Then, the particle dynamics is advanced according to Eq. (10).

Here, we consider two cases: (i) ring structural transition due to changing amplitude of the quartic potential and (ii) properties of the cylindrical shell structure for various particle numbers, coupling, and curvature of the parabolic potential. The equilibrium state in each simulation run has been achieved using a Nose-Hoover thermostat [54,55]. The velocities were chosen to follow a Gaussian distribution corresponding to dust temperature T_d for the considered coupling parameter Γ. It should be noted that for each simulation run, the system reached the desired equilibrium temperature (verified by temperature fluctuations and energy plots) well in advance of the simulation time.

First, to study the ring structural transition, we fix all other parameters and gradually change the amplitude E_{r0} of the quartic potential. This is achieved by a succession of simulation runs. For each value of E_{r0}, the simulation is advanced until an equilibrium state is achieved. Then, the simulation is stopped, the potential amplitude is varied, and the simulation is advanced until a new equilibrium state is achieved. In these successive runs, the equilibrium particle positions at the last time step of one run are used as initial positions for the next run (with a new E_{r0}). The initial temperature remains the same for all simulation runs. The total sum of potential energy and kinetic energy is conserved in each individual run but varies from run to run due to the changing confinement potential energy.

Next, for fixed quartic potential parameters, we explore how the properties of the cylindrical shell structure change with particle number, coupling strength, and characteristics of the parabolic (vertical) potential well. First, we select a value of the quartic potential amplitude E_{r0} that results in the formation of a cylindrical shell structure for given initial particle number, coupling, and parabolic potential. After equilibrium is achieved, successive simulation runs are used to vary one parameter (particle number, coupling strength, or parabolic potential curvature), while all other parameters are fixed. In each case, the resulting formation of perfect or imperfect rings inside this shell structure is analyzed.

III. NUMERICAL SIMULATION, RESULTS, AND DISCUSSION

All simulations have been carried out using the open-source MD code LAMMPS [56]. Boundary conditions are periodic in the xy plane and nonperiodic in the z direction. For all simulations, we consider a 3D simulation box of $lx\,(= 1\,\text{cm}) \times ly\,(= 1\,\text{cm}) \times lz\,(= 1\,\text{cm})$. lx, ly, and lz are the system lengths in the x, y, and z directions, respectively. Here, $-0.5 \leqslant x \leqslant 0.5$, $-0.5 \leqslant y \leqslant 0.5$, and $0 \leqslant z \leqslant 1$. Each dust particle has the same charge $Q = 11940\,e^-$ and same mass $m_d = 6.99 \times 10^{-10} g$. The confining quartic potential has a ring-shaped minimum along the radial distance $d = 0.3535\,\text{cm}$, located between the central barrier at $r = 0\,\text{cm}$ and the radial edge at $r = 0.5\,\text{cm}$. We have considered a constant value of

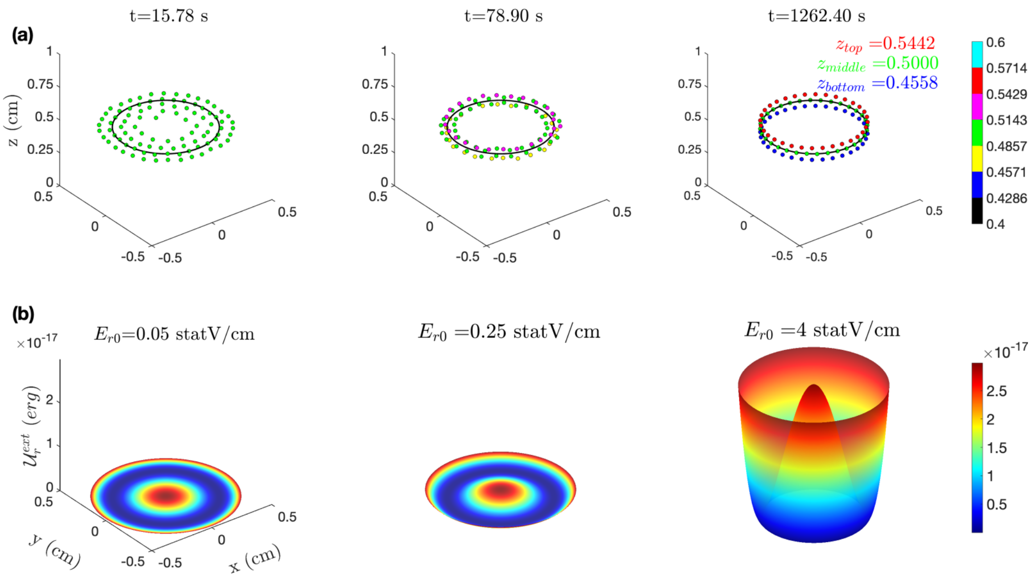

FIG. 3. Three equilibrium stages of the ring structural transition are represented in (a) under the influence of the increasing amplitude of the ring-shaped quartic potential shown in (b).

gravitational acceleration, $g = 981\,\mathrm{cm/s^2}$. The other parameters are chosen according to the specific problem.

A. Ring structure transition

Keeping in mind the cylindrical symmetry of the quartic potential, at $t = 0$, 96 $(= 3\times32)$ dust particles are randomly dispersed in a cylindrical volume of radius $r = 0.5$ cm centered around (0,0) and extending on the z axis from $z = 0.4$ cm to $z = 0.6$ cm within the simulation box. The coupling parameter is $\Gamma = 200$ and the respective dust kinetic temperature $T_d = Q^2/ak_B\Gamma = 1.404$ eV. With typical inter-dust distance $a = 7.31\times10^{-2}$cm and $\kappa = a/\lambda_D = 1.0$, the corresponding value of the Debye length is $\lambda_D = 7.31\times10^{-2}$cm. The characteristic frequency of the dust particles is $\omega_{pd} = 4\pi n_d Q^2/m_d{\sim}19.0\,\mathrm{s}^{-1}$, which corresponds to the dust plasma period of 0.331 s $(= 2\pi/\omega_{pd})$. We have chosen a simulation time step of $\Delta t = 5\times10^{-3}\,\omega_{pd}^{-1}$ or $\Delta t = 2.63\times10^{-4}$ s so that the simulation can easily resolve all phenomena occurring at the dust response time scale.

These initial conditions were used to study the ring structural transition due to a gradual change in the amplitude of the quartic potential. For each value of the quartic potential, the simulation is run until an equilibrium state is achieved. Each simulation run has a total number of time steps $N_{\text{steps}} = 6\times10^4$, which corresponds to run time 15.78 s (i.e., $N_{\text{steps}}\times\Delta t$ s). After $t = 15.78$ s, the simulation is stopped and the amplitude of the quartic potential E_{r0} from Eq. (8) is changed. First, the amplitude is increased in 80 successive runs from $E_{r0} = 0.05$ statV/cm to a maximum value of $E_{r0} = 4$ statV/cm $(= 0.05\times80)$ at $t = 1262.4$ s. Then, for the next 79 runs, the amplitude is decreased by the same amount at the same time intervals to get back to $E_{r0} = 0.05$ statV/cm. In this section, the curvature of the parabolic potential is kept fixed at $c = -1.0$.

The three subplots in Fig. 3(a), from left to right, display the final thermal equilibrium of 96 dust particles for three representative values of the quartic potential well amplitude. The subplots in Fig. 3(b) show the shape of the corresponding potential well $\mathcal{U}_r^{\text{ext}}$ for each case. In Fig. 3(a), the locations of the quartic potential minima are marked by a black circle with radius $d = 0.3535$ cm at a vertical height $z = 0.5$ cm (minima of the parabolic potential). The colorbar in Fig. 3(a) corresponds to the vertical positions of the dust particles. In Fig. 3(b), the colorbar represents the magnitude of the quartic potential energy. During the first 15.78 s of the simulation, the dust particles form a *circular monolayer structure* under the action of the quartic potential with amplitude $E_{r0} = 0.05$ statV/cm. The monolayer consists of approximately four rings, nested within the same plane, which is visible by the same green color of the dots in the first subplot of Fig. 3(a). This circular structure has approximate symmetry about the $d = 0.3535$ cm and is located at a vertical height $z = 0.5$ cm because the net quartic potential force points in the direction of the minimum (as discussed in Sec. II). The dust particles will remain within the plane if their planar interparticle separation is sufficient for the dust-dust interaction force to balance the confinement force from the quartic potential.

The particle positions of this circular monolayer structure have been used as the initial positions for the next simulation (from $t = 15.78$ s to $t = 31.56$ s) during which the quartic potential amplitude is increased from 0.05 statV/cm to $E_{r0} = 0.1$ statV/cm. Higher E_{r0} value causes stronger radial force which radially squeezes the dust particle structure around the potential well's minimum. The central barrier of the potential pushes the ring of the innermost particles toward the minimum, while the circular edge pushes the ring of the outermost particles toward the minimum. The competition between the radial potential (due to the increase in amplitude) and the dust-dust interactions results in irregularities in the coplanner rings both in the horizontal (perpendicular to gravity) and vertical (parallel to gravity) directions.

At the later time $t = 78.90$ s, as the net confinement force increases by increasing the amplitude to $E_{r0} = 0.25$ statV/cm,

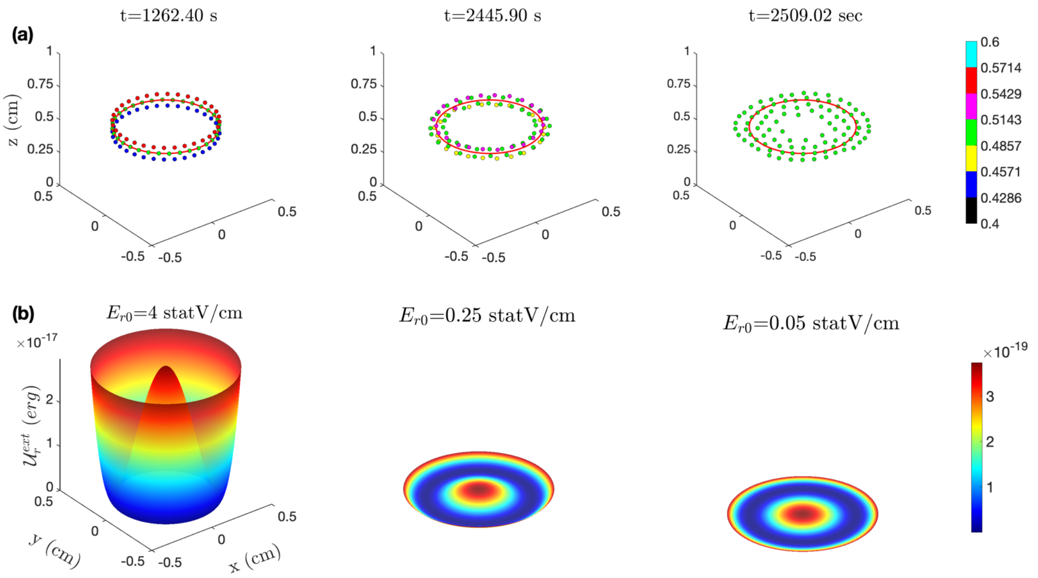

FIG. 4. Three equilibrium stages of the ring structural transition are represented in subplot (a) under the influence of the decreasing amplitude of the ring-shaped quartic potential shown in subplot (b).

the middle two rings shift along the vertical z axis, one toward the bottom (yellow dots), and one toward the top (magenta dots). The innermost ring (which now has larger radius than earlier at $t = 15.78$ s) and outermost ring (which now has smaller radius than earlier at $t = 15.78$ s) remain nearly coplanar (green dots) at the same vertical height $z = 0.5$ cm. We refer to this arrangement of dust particles as a *transitional structure state*. An expanded image of the transitional structure state is shown in Fig. 5(b).

Further increasing the value of E_{r0} eventually leads to a structure in which the dust particles are aligned in rings with the same diameter, located one above the other within a cylindrical surface. At $t = 1262.4$ s, when the potential amplitude is $E_{r0} = 4$ statV/cm, the particles settle in three perfect rings with a radius of 0.3535 cm: the top one at $z = 0.5442$ cm (red dots), the middle one at $z = 0.5$ cm (green dots), and the bottom one at $z = 0.4558$ cm (blue dots). We refer to this state as a *cylindrical shell structure*, where each of the three rings has an equal number of dust particles (here, 32). Subsequent simulation runs with a higher potential amplitude do not yield discernible changes to the cylindrical ring structure. All transitional states in between the circular monolayer structure and cylindrical shell structure consist of irregular rings that manifest zigzag instabilities in both the horizontal and vertical directions.

To test the reversibility of this structure transition phenomenon, we repeat the simulation from $t = 1262.4$ s to $t = 2509.02$ s, this time decreasing the amplitude value from $E_{r0} = 4$ statV/cm to $E_{r0} = 0.05$ statV/cm by the same amount of 0.05 statV/cm at the same interval of time (= 15.78 s) for each simulation run. The outcomes of this simulation are shown in Fig. 4. Based on a visual comparison of subplots, the formation of structures in Fig. 4(a) appears to be similar to that in Fig. 3(a) for the same values of E_{r0}. Thus, we find

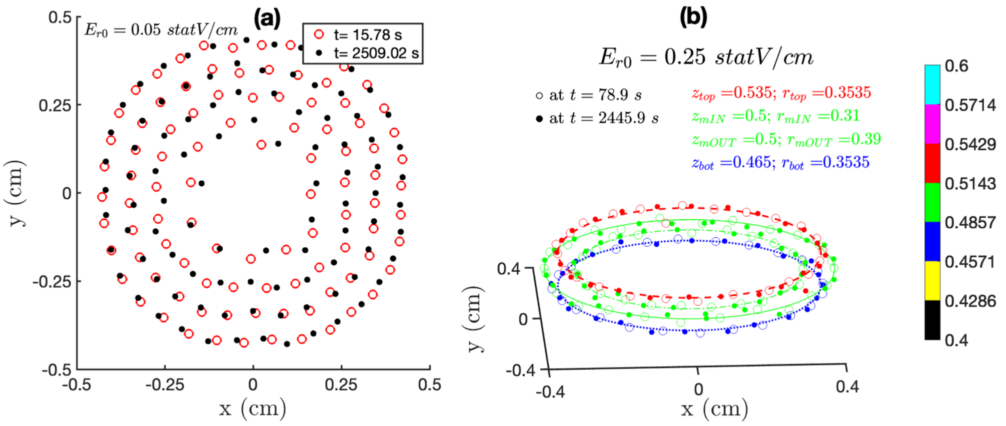

FIG. 5. Comparison of the dust position distributions from the forward and backward simulations for corresponding values of E_{r0}. The plot in (a) shows the distribution of particle positions for $t = 15.78$ s [red circles, Fig. 3(a)] along with the distribution at $t = 2509.02$ s [black dots, Fig. 4(a)]. The plot in (b) shows the distribution of particle positions for $t = 78.90$ s [multicolor circles, Fig. 3(a)] along with the distribution at $t = 2445.90$ [multicolor dots, Fig. 4(a)]. Colorbar in the right panel corresponds to the vertical locations (z) of the particles.

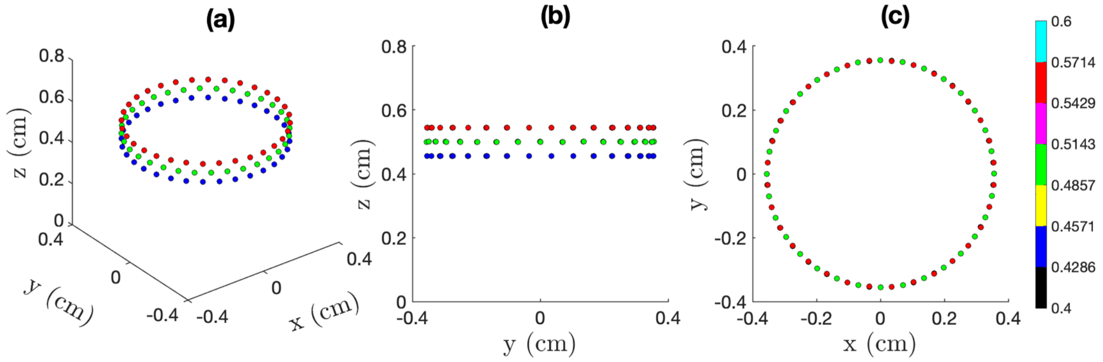

FIG. 6. The dust particles within the cylindrical surface structure arrange in a regular hexagonal pattern for $E_{r0} = 4.0$ statV/cm (data from $t = 1262.40$ s). The figure panels [Figs. 3(c) and 4(a)] show three different views: (a) 3D view, (b) yz plane, and (c) xy plane.

that this structure transition is reversible in terms of layer or ring formation.

As we mentioned above, in each successive run, the final particle positions of the previous state have been used as the initial positions for the next one. This means that during the backward and forward simulations, the initial particle positions were not the same for the same E_{r0}. For example, during the forward run for $E_{r0} = 0.05$ statV/cm [at $t = 15.78$ s in Fig. 3(a)], the initial particle positions were random, while during the backward run, the initial particle positions for $E_{r0} = 0.05$ statV/cm [at $t = 2445.9$ s in Fig. 4(a)] belong to the previous state for $E_{r0} = 0.1$ statV/cm (at $t = 2493.42$ s). Therefore, it is expected that the equilibrium particle distributions for forward and backward runs with the same E_{r0} will differ.

Figure 5 shows the equilibrium states from the forward and backward simulation runs with the same E_{r0}. The distribution of dust particles at $t = 15.78$ s (Fig. 3(a)] from the forward simulation is represented by red circles (○), while the distribution of particles at $t = 2509.02$ s [Fig. 4(a)] from the backward simulation is represented by black dots (●) together in Fig. 5(a). We see that, although both simulations resulted in circular monolayer structures, the distribution of final particle positions is different. This is due to the differences in initial distributions of particle positions in each simulation. A similar trend is observed for transitional states. In Fig. 5(b), the distribution of dust particles from the forward simulation [represented by the multicolored circles (○)] at $t = 78.9$ s [Fig. 3(a)] has been plotted over the distribution of particles from the backward simulation [represented by multicolored dots (●)] at time $t = 2445.9$ s [Fig. 4(a)]. It is again visible that particle locations are not exactly the same under the same external potential $E_{r0} = 0.25$ statV/cm. In Fig. 5(b), we have highlighted the four rings with solid circles based on their radii and vertical positions: the bottom (blue: radius $r_{\text{bot}} = 0.3535$ cm and vertical location $z_{\text{bot}} = 0.465$ cm), the top (red: radius $r_{\text{top}} = 0.3535$ cm and vertical location $z_{\text{top}} = 0.535$ cm), and the two middle rings (green: radii of the inner ($r_{m\text{IN}} = 0.31$ cm) and outer $r_{m\text{OUT}} = 0.39$ cm, and same vertical location $z_{m\text{IN}} = z_{m\text{OUT}} = 0.5$ cm). Thus, we conclude that the ring structural transition exhibits hysteresis in the particle positions.

Another interesting observation is that within the cylindrical shell structure, the dust particles arrange in a hexagonal lattice structure, as shown in Fig. 6. Figures 6(a) (3D view) and 6(b) (yz plane). The z position of the top ring particles (red dots) aligns with the z position of the bottom ring particles (blue dots), while the middle ring particles (green dots) are located in between. If the number of particles in the simulation is increased enough so that more rings are added to the cylindrical shell structure, the symmetry in vertical alignment will repeat, forming an A-B-A-B-A-B structure [the curvature of the parabolic potential (causes for the vertical confinement) may also affect this structure].

Figure 7 shows the same simulation experiment repeated with a smaller number of particles. Figure 7(a) depicts a ring structural transition for 64 (= 2×32) dust particles. The cylindrical shell structure in this case is made up of two perfect rings, each with 32 particles, where the top ring particles (red dots) settle in between the bottom ring particles (blue dots). Figure 7(b) depicts a 32 (= 1×32) particle with a single perfect ring at the maximum value of the potential amplitude.

B. Parametric dependency in the formation of the cylindrical shell structure

In addition to the amplitude value E_{r0}, the number of dust particles N (or number density), the screening parameter κ, and the control parameter c for parabolic potential $\mathcal{U}_z^{\text{ext}}$, all play a crucial role in the formation of the observed dust structures. To investigate the role of these parameters, all results in this section were obtained from a single simulation period (0 s to 15.78 s) with fixed amplitude $E_{r0} = 4.0$ statV/cm. The initial state is a random distribution of dust particles which forms a cylindrical shell structure at equilibrium for the chosen amplitude $E_{r0} = 4.0$ statV/cm. To ensure that the particles are distributed uniformly within each ring and to prevent a zigzag instability or ring irregularities in the cylindrical shell structure, the number of particles should be divisible by the number of rings. We have summarized some findings regarding the formation of perfect or imperfect rings in the cylindrical shell structures as different parameters are varied: Fig. 8 (changing N for constant $\kappa = 1$ and $c = -1$), Fig. 9 (changing κ for constant $c = -10$ and $N = 72$), and Fig. 10 (changing c for constant $\kappa = 1$ and $N = 72$) for a fixed value of $E_{r0} = 4.0$ statV/cm.

Figure 8 shows the results for different numbers of dust particles N with fixed values of $\kappa = 1$ and $c = -1$. As

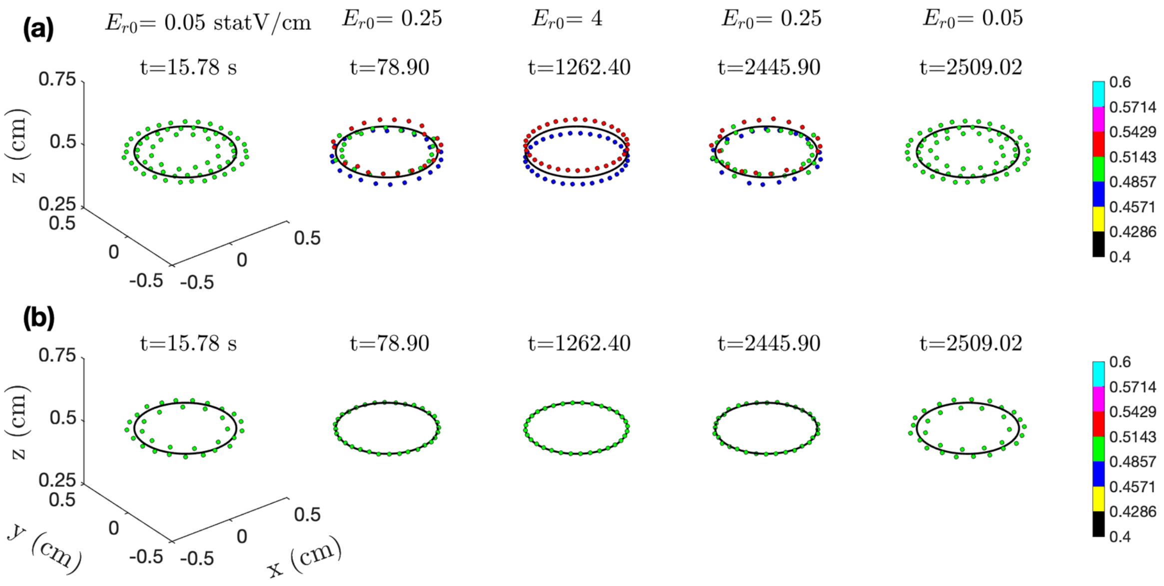

FIG. 7. The ring structural transition for (a) 64 (= 2×32) and (b) 32 (= 1×32) dust particles due to the change in E_{r0}.

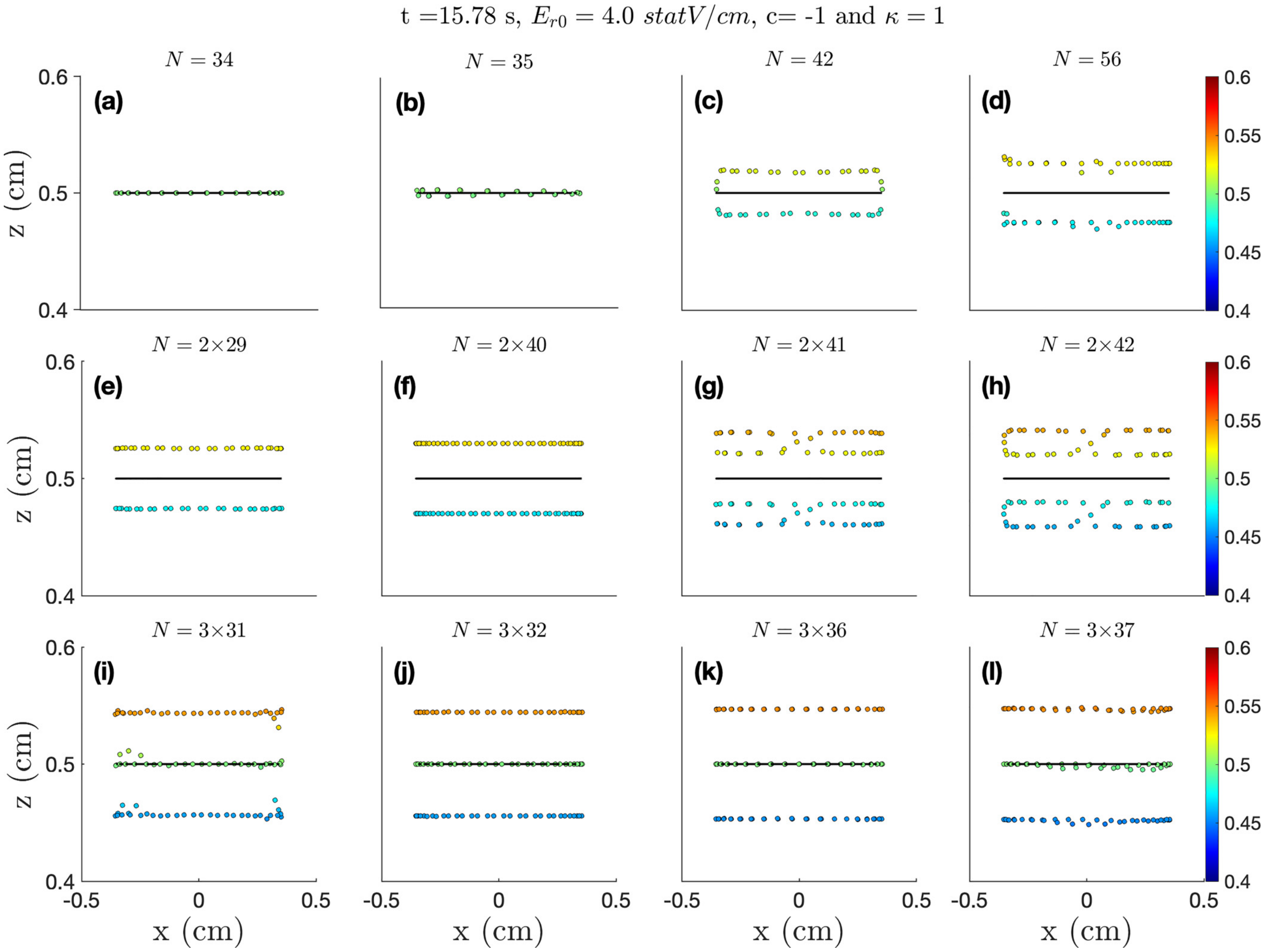

FIG. 8. Ring structure formation in the cylindrical surface state for different number of dust particles N. All subplots show the equilibrium structure at $t = 15.78$ s with fixed values of $E_{r0} = 4.0$ statV/cm, κ=1, and $c = -1$.

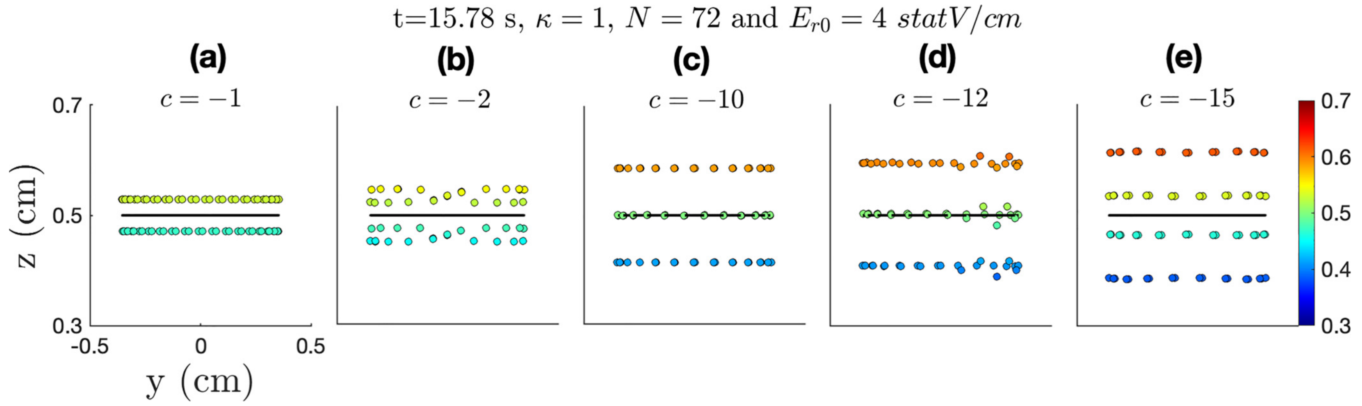

FIG. 9. Ring structure formation in the cylindrical surface state for different κ. All subplots show the equilibrium structure at $t = 15.78$ s with fixed values of $E_{r0} = 4.0$ statV/cm, number of particles $N = 72$, and $c = -10$.

illustrated in Fig. 8(a), particle numbers up to 34 arrange into a single perfect ring with radius $d = 0.3535$ cm, located at vertical equilibrium height $z = 0.5$ cm. As the density of the dust particles increases, the interparticle separation decreases and the repulsive Yukawa interaction becomes more pronounced. Since there is no more room to expand radially within the same plane, further increasing N results in the extension of existing rings vertically with some irregularities and, eventually, in the formation of a new ring. Thus, with the addition of one more particle to the 34-particle ring, the structure becomes irregular due to a zigzag instability, as displayed in Fig. 8(b). Further addition of particles leads to the formation of a new ring located at a different vertical height. Initially two irregular rings are formed that attempt to balance vertically: one shifts lower and the other shifts higher with respect to the vertical equilibrium location $z = 0.5$ cm, as shown in Figs. 8(c) and 8(d). Finally, two perfect rings are observed for particle numbers ranging from $N = 58 = 2\times29$ up to $N = 80 = 2\times40$, as shown in Figs. 8(e) and 8(f). The addition of more particles results in the formation of an additional ring through similar intermediate irregular structures [Figs. 8(g)–8(i)]. The formation of three perfect rings is observed for particle numbers ranging from $N = 96 = 3\times32$ to $N = 108 = 3\times36$, as shown in Figs. 8(j) and 8(k). The formation of additional rings via irregular intermediate structures is repeated if more particles are added to the current system [Fig. 8(l)].

The snapshots in Fig. 9 represent the equilibrium configurations of 72 particles for different κ at $t = 15.78$ s. The values of $E_{r0} = 4$ statV/cm and $c = -10$ are constant. Figure 9(a) shows that two perfect rings, made of 36 particles each, form for $\kappa = 5$. The parameter κ is the ratio of average interparticle separation to the Debye screening length. Thus, it quantifies the characteristic spatial scale at which the Yukawa interaction acts. As κ is decreased, the range of repulsive interactions among dust particles increases. For $E_{r0} = 4$ statV/cm it is not favorable for the dust particles to spread in the radial direction. Therefore, the effect of decreasing κ can either lead to expanding the dust interparticle separation vertically, which results in ring irregularities, or to producing a new ring at a different vertical height. Figure 9(b) shows the formation of irregularities in the existing two rings as they try to form a third ring for $\kappa = 3$. Finally, three perfect rings are observed to form for $\kappa = 1$, as shown in Fig. 9(b), with each ring containing 24 particles ($N = 72 = 3\times24$). The formation of a forth ring through intermediate irregular states is repeated as the value of κ is further decreased, as shown in Figs. 9(d) and 9(e). It should be emphasized that in this case, the value of c must favor the addition of a new ring to the given structure. If $c = -1$, we don't see this transition event.

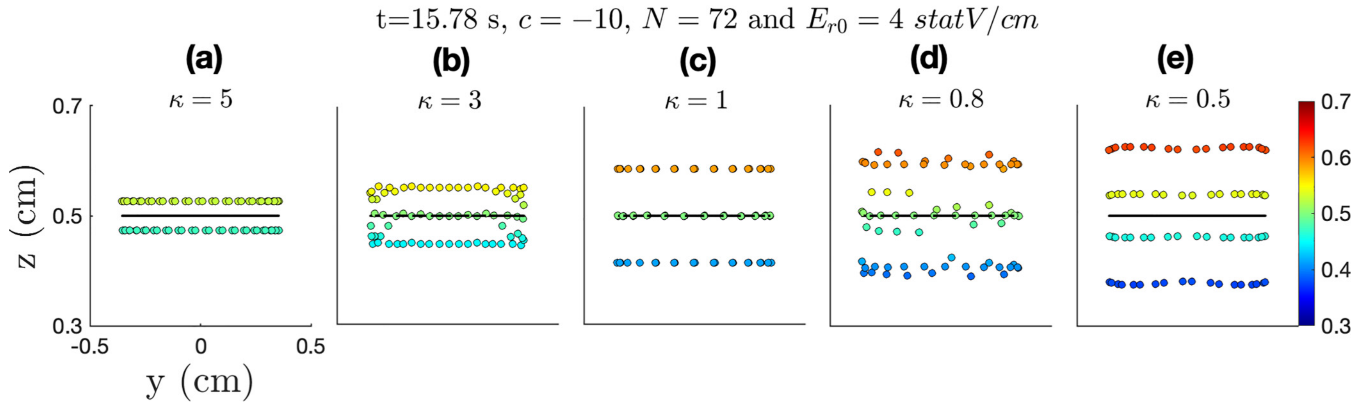

FIG. 10. Ring structure formation in the cylindrical surface state for different c. All subplots show the equilibrium structure at $t = 15.78$ s with fixed values of $E_{r0} = 4.0$ statV/cm; number of particles $N = 72$, and $\kappa = 1$ are kept constant.

TABLE I. Ring structure formation in the cylindrical shell state for different numbers of dust particles for $c = -5$ and $c = -10$.

c No. of rings	$c = -5$	$c = -10$
1	Up to 23	Up to 19
2	32 (= 2×16) to 54 (= 2×27)	24 (= 2×12) to 44 (= 2×22)
3	60 (= 3×20) to 78 (= 3×26)	51 (= 3×17) to 72 (= 3×24)
4	96 (= 4×24)	84 (= 4×21) to 92 (= 4×23)
5		125 (= 5×25) to 130 (= 5×26)

Figure 10 shows equilibrium configurations of 72 particles for different c values with fixed values of $E_{r0} = 4$ statV/cm and $\kappa = 1$ at $t = 15.78$ s. For $c = -1$, two perfect rings are observed, as shown in Fig. 10(a), and each of the rings has an equal number of dust particles, 36. The parameter c controls the curvature of the parabolic potential whose axis of symmetry is perpendicular to the gravitational force and centered on the equilibrium vertical position $z = 0.5$. When c decreases, the curvature of the parabolic confining potential becomes less steep, increasing the amount of vertical space available for the particles. This can either cause growing irregularities between neighboring rings or result in the formation of new rings. Figure 10(b) shows that for $c = -2$, the interparticle separation in the existing two rings increases in the vertical direction resulting in irregular structure. For $c = -10$, Fig. 9(c) depicts the formation of a third ring, with each ring containing 24 particles ($N = 72 = 3\times24$). If the value of c is further decreased, additional rings are formed through intermediate irregular states, as shown in Figs. 10(d) and 10(e).

Table I provides a summary of results for simulations with different numbers of dust particles N with fixed values of $\kappa = 1$. The range of perfect ring formation has is shown by rows for $c = -5$ and $c = -10$.

IV. CONCLUSIONS AND OUTLOOK

In dusty plasmas, the competition between interaction potential forces and external confinement forces can lead to the formation of interesting structural states and structural transitions. To explore the ring structural transition in a dusty plasma, we conducted MD simulations where charged dust particles are confined in a ring-shaped quartic potential well. Here we presented the results from two cases. In the first case, we examined how increasing the value of the quartic potential amplitude can lead to the transition from a ring monolayer structure (rings of different diameters nested within the same plane) to a cylindrical shell structure (rings of similar diameter aligned in parallel planes). We established that the ring structure transition occurs through several transitional states where the rings exhibit irregularities and zigzag instabilities. The transition is also reversible, but shows hysteresis in the initial and final distributions of particle positions. In the cylindrical surface structure, the particles are arranged in a perfect hexagonal pattern, with each ring containing an equal number of particles.

In the second case, we investigated how the ring formation within the cylindrical surface structure state depends on the number of dust particles N, the screening parameter κ, and the curvature of the parabolic potential (denoted by the parameter c) for a fixed value of $E_{r0} = 4$ statV/cm. For this high value of the quartic potential amplitude it is not energetically favorable for the particles to move in the radial direction; the effect of the above parameters results either in the formation of ring irregularities due to increased particle separation in the vertical direction, or in the formation of new rings at different vertical height. Therefore, as κ decreases, c decreases, and/or the number density increases, we observe the formation of additional rings within the cylindrical shell through several intermediate states with irregularities solely in the vertical direction.

We suggest that the present configuration (duty plasma confined in a quartic potential well) can be used to explore various fundamental phenomena. For example, in a laboratory experiment where the quartic potential is achieved by a combination of rings on the lower electrode and/or weak magnetic field, rapid variations of the electrodes power can be used to cause implosion or explosion of the annular dust structure that would allow the exploration of various phenomena, including acoustic waves, two-stream instabilities, bump-on-tail instabilities, spatial variation in coupling strength, and much more. This has been previously shown for sculpted ultracold neutral plasmas in [57]. Since the transition from a ring monolayer to a cylindrical shell structure is highly sensitive to the dust interaction potential, we further conjecture that it can be used to investigate the dust particle charging in laboratory settings. Finally, we would like to add that since this ring-shaped potential looks like a Mexican hat, this potential is also referred to as the "Mexican hat potential" [58,59]. For a system consisting of classical particles in such a Mexican hat potential might be a nice model for symmetry breaking via the Goldstone mechanism [60,61].

ACKNOWLEDGMENTS

This work is supported by NSF 1903450 and NSF OIA-2148653 (EPSCoR FTTP).

APPENDIX: THE STRUCTURE TRANSITION FROM A CYLINDRICAL SHELL TO A CIRCULAR MONOLAYER AND AGAIN TO A CYLINDRICAL SHELL

In the following Fig. 11, we compute the 96 random dust particle system with the change in trend of E_{r0} which is reversed from the previously discussed case in Figs. 3 and 4. This means that the starting amplitude is the highest, $E_{r0} = 4$ statV/cm, then decreases to the lowest, $E_{r0} = 0.05$ statV/cm, and then begins to increase to $E_{r0} = 4$ statV/cm. Apart from

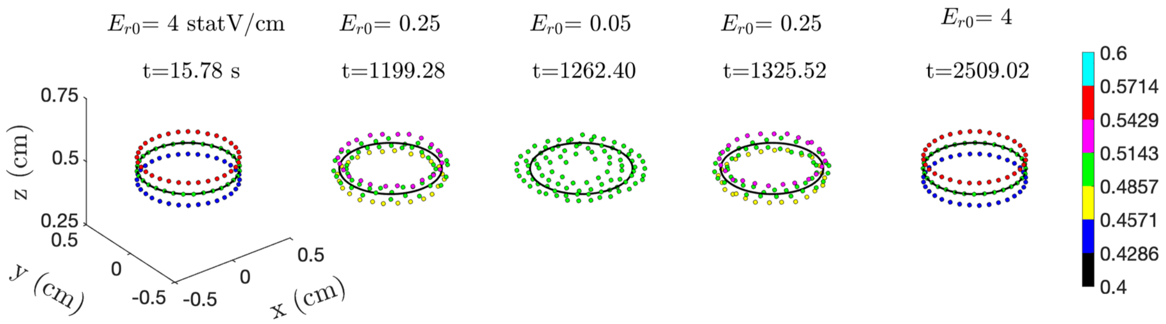

FIG. 11. A ring structural transition phenomenon under containment swinging potential well. There is an initial decrease in magnitude of quartic potential well and then an increase in the magnitude.

the reverse order of the amplitude of potential, all other conditions are similar. In Fig. 11, as expected, all five subplots show the transformation from a cylindrical shell structure ($E_{r0} = 4\,\text{statV/cm}$) to a circular monolayer structure ($E_{r0} = 0.05\,\text{statV/cm}$) and again to a cylindrical shell structure ($E_{r0} = 4\,\text{statV/cm}$) through various transition states.

[1] S. Ichimaru, Strongly coupled plasmas: High-density classical plasmas and degenerate electron liquids, Rev. Mod. Phys. **54**, 1017 (1982).

[2] N. N. Rao, P. K. Shukla, and M. Yu. Yu, Dust-acoustic waves in dusty plasmas, Planet. Space Sci. **38**, 543 (1990).

[3] J. X. Ma, Jin-yuan Liu, and M. Y. Yu, Fluid theory of the boundary of a dusty plasma, Phys. Rev. E **55**, 4627 (1997).

[4] P. K. Kaw and A. Sen, Low frequency modes in strongly coupled dusty plasmas, Phys. Plasmas **5**, 3552 (1998).

[5] V. Singh Dharodi, S. Kumar Tiwari, and A. Das, Visco-elastic fluid simulations of coherent structures in strongly coupled dusty plasma medium, Phys. Plasmas **21**, 073705 (2014).

[6] A. Diaw and M. S. Murillo, Generalized hydrodynamics model for strongly coupled plasmas, Phys. Rev. E **92**, 013107 (2015).

[7] V. S. Dharodi, Rotating vortices in two-dimensional inhomogeneous strongly coupled dusty plasmas: Shear and spiral density waves, Phys. Rev. E **102**, 043216 (2020).

[8] H. Ikezi, Coulomb solid of small particles in plasmas, Phys. Fluids **29**, 1764 (1986).

[9] H. Thomas, G. E. Morfill, V. Demmel, J. Goree, B. Feuerbacher, and D. Möhlmann, Plasma Crystal: Coulomb Crystallization in a Dusty Plasma, Phys. Rev. Lett. **73**, 652 (1994).

[10] J. H. Chu and I. Lin, Direct Observation of Coulomb Crystals and Liquids in Strongly Coupled rf Dusty Plasmas, Phys. Rev. Lett. **72**, 4009 (1994).

[11] Y. Hayashi and K. Tachibana, Observation of coulomb-crystal formation from carbon particles grown, Jpn. J. Appl. Phys. **33**, L804 (1994).

[12] L. Bin, L. Yan-Hong, C. Yan-Ping, Y. Si-Ze, and W. Long, Structure and phase transition of a two-dimensional dusty plasma, Chin. Phys. **12**, 765 (2003).

[13] A. Melzer, A. Schella, T. Miksch, J. Schablinkski, D. Block, A. Piel, H. Thomsen, H. Kählert, and M. Bonitz, Phase transitions of finite dust clusters in dusty plasmas, Contrib. Plasma Phys. **52**, 795 (2012).

[14] S. Maity and A. Das, Molecular dynamics study of crystal formation and structural phase transition in yukawa system for dusty plasma medium, Phys. Plasmas **26**, 023703 (2019).

[15] V. S. Dharodi and A. Das, A numerical study of gravity-driven instability in strongly coupled dusty plasma. Part 1. Rayleigh–Taylor instability and buoyancy-driven instability, J. Plasma Phys. **87**, 905870216 (2021).

[16] V. S. Dharodi, A numerical study of gravity-driven instability in strongly coupled dusty plasma. Part 2. Hetero-interactions between a rising bubble and a falling droplet, J. Plasma Phys. **87**, 905870402 (2021).

[17] S. K. Tiwari, V. S. Dharodi, A. Das, B. G. Patel, and P. Kaw, Evolution of sheared flow structure in visco-elastic fluids, in *Proceedings of the International Conference on Complex Processes in Plasmas and Nonlinear Dynamical Systems*, edited by A. Das and A. S. Sharma (American Institute of Physics, 2014), Vol. 1582, pp. 55–65.

[18] S. Tiwari, V. Dharodi, A. Das, P. Kaw, and A. Sen, Kelvin-helmholtz instability in dusty plasma medium: Fluid and particle approach, J. Plasma Phys. **80**, 817 (2014).

[19] V. S. Dharodi, B. Patel, and A. Das, Kelvin–Helmholtz instability in strongly coupled dusty plasma with rotational shear flows and tracer transport, J. Plasma Phys. **88**, 905880103 (2022).

[20] A. Gupta, R. Ganesh, and A. Joy, Kolmogorov flow in two dimensional strongly coupled dusty plasma, Phys. Plasmas **21**, 073707 (2014).

[21] S. Zhdanov, M. Schwabe, C. Räth, H. M. Thomas, and G. E. Morfill, Wave turbulence observed in an auto-oscillating complex (dusty) plasma, Europhys. Lett. **110**, 35001 (2015).

[22] S. K. Tiwari, V. S. Dharodi, A. Das, B. G. Patel, and P. Kaw, Turbulence in strongly coupled dusty plasmas using generalized hydrodynamic description, Phys. Plasmas **22**, 023710 (2015).

[23] E. G. Kostadinova, R. Banka, J. L. Padgett, C. D. Liaw, L. S. Matthews, and T. W. Hyde, Fractional laplacian spectral approach to turbulence in a dusty plasma monolayer, Phys. Plasmas **28**, 073705 (2021).

[24] R. L. Merlino, 25 years of dust acoustic waves, J. Plasma Phys. **80**, 773 (2014).

[25] V. Dharodi, A. Das, B. Patel, and P. Kaw, Sub-and superluminar propagation of structures satisfying poynting-like theorem for incompressible generalized hydrodynamic fluid

model depicting strongly coupled dusty plasma medium, Phys. Plasmas **23**, 013707 (2016).

[26] E. G. Kostadinova, F. Guyton, A. Cameron, K. Busse, C. Liaw, L. S. Matthews, and T. W. Hyde, Transport properties of disordered two-dimensional complex plasma crystal, Contrib. Plasma Phys. **58**, 209 (2018).

[27] M. Schwabe, U. Konopka, P. Bandyopadhyay, and G. E. Morfill, Pattern Formation in a Complex Plasma in High Magnetic Fields, Phys. Rev. Lett. **106**, 215004 (2011).

[28] E. Thomas, Jr., B. Lynch, U. Konopka, R. L. Merlino, and M. Rosenberg, Observations of imposed ordered structures in a dusty plasma at high magnetic field, Phys. Plasmas **22**, 030701 (2015).

[29] E. Thomas, R. L. Merlino, and M. Rosenberg, Magnetized dusty plasmas: The next frontier for complex plasma research, Plasma Phys. Controlled Fusion **54**, 124034 (2012).

[30] U. Konopka, D. Samsonov, A. V. Ivlev, J. Goree, V. Steinberg, and G. E. Morfill, Rigid and differential plasma crystal rotation induced by magnetic fields, Phys. Rev. E **61**, 1890 (2000).

[31] M. Choudhary, R. Bergert, S. Mitic, and M. H. Thoma, Three-dimensional dusty plasma in a strong magnetic field: Observation of rotating dust tori, Phys. Plasmas **27**, 063701 (2020).

[32] N. Chaubey and J. Goree, Preservation of a dust crystal as it falls in an afterglow plasma, Front. Phys. **10**, 879092 (2022).

[33] B. Liu, K. Avinash, and J. Goree, Transverse Optical Mode in a One-Dimensional Yukawa Chain, Phys. Rev. Lett. **91**, 255003 (2003).

[34] T. E. Sheridan and K. D. Wells, Dimensional phase transition in small yukawa clusters, Phys. Rev. E **81**, 016404 (2010).

[35] F. Huang, Y.-H. Liu, Z.-Y. Chen, L. Wang, and M.-F. Ye, Cluster rotation in an unmagnetized dusty plasma, Chin. Phys. Lett. **30**, 115201 (2013).

[36] P. Hartmann, J. C. Reyes, E. G. Kostadinova, L. S. Matthews, T. W. Hyde, R. U. Masheyeva, K. N. Dzhumagulova, T. S. Ramazanov, T. Ott, H. Kählert *et al.*, Self-diffusion in two-dimensional quasimagnetized rotating dusty plasmas, Phys. Rev. E **99**, 013203 (2019).

[37] K. Qiao and T. W. Hyde, Structure and vertical modes in finite 2d plasma crystals, in *2007 16th IEEE International Pulsed Power Conference* (IEEE, 2007), Vol. 2, pp. 1441–1444.

[38] I. V. Schweigert, V. A. Schweigert, and F. M. Peeters, Properties of two-dimensional coulomb clusters confined in a ring, Phys. Rev. B **54**, 10827 (1996).

[39] T. E. Sheridan, Dusty plasma ring model, Phys. Scr. **80**, 065502 (2009).

[40] T. E. Sheridan and J. C. Gallagher, Dusty plasma (yukawa) rings, Phys. Plasmas **23**, 110703 (2016).

[41] W. L. Theisen and M. J. Sibila, Rotating one ring in an unmagnetized dusty plasma, IEEE Trans. Plasma Sci. **48**, 2873 (2020).

[42] Ya-feng He, Bao-quan Ai, Chao-xing Dai, C. Song, Rui-qi Wang, Wen-tao Sun, Fu-cheng Liu, and Y. Feng, Experimental Demonstration of a Dusty Plasma Ratchet Rectification and Its Reversal, Phys. Rev. Lett. **124**, 075001 (2020).

[43] A. Melzer, Zigzag transition of finite dust clusters, Phys. Rev. E **73**, 056404 (2006).

[44] P. K. Shukla and A. A. Mamun, *Introduction to Dusty Plasma Physics* (CRC press, 2015).

[45] N. Chaubey, J. Goree, S. J. Lanham, and M. J. Kushner, Positive charging of grains in an afterglow plasma is enhanced by ions drifting in an electric field, Phys. Plasmas **28**, 103702 (2021).

[46] N. Chaubey and J. Goree, Coulomb expansion of a thin dust cloud observed experimentally under afterglow plasma conditions, Phys. Plasmas **29**, 113705 (2022).

[47] S. Hamaguchi, R. T. Farouki, and D. H. E. Dubin, Triple point of yukawa systems, Phys. Rev. E **56**, 4671 (1997).

[48] G. I. Sukhinin, A. V. Fedoseev, T. S. Ramazanov, R. Zh. Amangaliyeva, M. K. Dosbalayev, and A. N. Jumabekov, Nonlocal effects in a stratified glow discharge with dust particles, J. Phys. D **41**, 245207 (2008).

[49] K. Qiao and T. W. Hyde, Structural phase transitions and out-of-plane dust lattice instabilities in vertically confined plasma crystals, Phys. Rev. E **71**, 026406 (2005).

[50] T. W. Hyde, J. Kong, and L. S. Matthews, Helical structures in vertically aligned dust particle chains in a complex plasma, Phys. Rev. E **87**, 053106 (2013).

[51] E. B. Tomme, D. A. Law, B. M. Annaratone, and J. E. Allen, Parabolic Plasma Sheath Potentials and their Implications for the Charge on Levitated Dust Particles, Phys. Rev. Lett. **85**, 2518 (2000).

[52] H. Totsuji, T. Kishimoto, and C. Totsuji, Structure of Confined Yukawa System (Dusty Plasma), Phys. Rev. Lett. **78**, 3113 (1997).

[53] H. T. H. Totsuji, T. K. T. Kishimoto, and C. T. C. Totsuji, Structure of dusty plasma in external fields: Simulation and theory, Jpn. J. Appl. Phys. **36**, 4980 (1997).

[54] S. Nosé, A molecular dynamics method for simulations in the canonical ensemble, Mol. Phys. **52**, 255 (1984).

[55] W. G. Hoover, Canonical dynamics: Equilibrium phase-space distributions, Phys. Rev. A **31**, 1695 (1985).

[56] S. Plimpton, Fast parallel algorithms for short-range molecular dynamics, J. Comput. Phys. **117**, 1 (1995).

[57] V. S. Dharodi and M. S. Murillo, Sculpted ultracold neutral plasmas, Phys. Rev. E **101**, 023207 (2020).

[58] J. Goldstone, Field theories with «superconductor» solutions, Il Nuovo Cim. **19**, 154 (1961).

[59] N. Mee, *Higgs Force: The Symmetry-Breaking Force that Makes the World an Interesting Place* (James Clarke & Co., 2012).

[60] J. Ellis, M. K. Gaillard, and D. V. Nanopoulos, A historical profile of the higgs boson, *The Standard Theory of Particle Physics* (World Scientific, 2016), pp. 255–274.

[61] Q. N. Meier, A. Stucky, J. Teyssier, S. M. Griffin, D. Van Der Marel, and N. A. Spaldin, Manifestation of structural higgs and goldstone modes in the hexagonal manganites, Phys. Rev. B **102**, 014102 (2020).